

RESEARCH ARTICLE | DECEMBER 15 2023

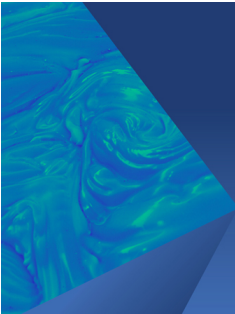
Effects of micrometer-scale cavities on the shock-to-detonation transition in a heterogeneous LX-17 energetic material

Jie Sun ; Pengfei Yang ; Baoqing Meng  ; Rui Zhou ; Baolin Tian ; Zheng Chen 



Physics of Fluids 35, 126117 (2023)


<https://doi.org/10.1063/5.0174851>



Physics of Fluids

Special Topic:
John Michael Dealy (1937-2024): Celebrating His Life
Guest Editors: Alan Jeffrey Giacomini and Savvas G. Hatzikiriakos

[Submit Today!](#)



Effects of micrometer-scale cavities on the shock-to-detonation transition in a heterogeneous LX-17 energetic material

Cite as: Phys. Fluids **35**, 126117 (2023); doi: [10.1063/5.0174851](https://doi.org/10.1063/5.0174851)

Submitted: 3 September 2023 · Accepted: 30 November 2023 ·

Published Online: 15 December 2023



View Online



Export Citation



CrossMark

Jie Sun,¹ Pengfei Yang,² Baoqing Meng,^{2,a)} Rui Zhou,³ Baolin Tian,^{1,3} and Zheng Chen¹

AFFILIATIONS

¹HEDPS, CAPT, SKLTCS, College of Engineering, Peking University, Beijing 100871, China

²State Key Laboratory of High Temperature Gas Dynamics, Institute of Mechanics, Chinese Academy of Sciences, Beijing 100190, China

³LCP, Institute of Applied Physics and Computational Mathematics, Beijing 100094, China

^{a)}Author to whom correspondence should be addressed: mengbaoqing92@foxmail.com

ABSTRACT

Cavities and other fracture structures within energetic materials may have significant impact on their performance. The mechanism on how hot spots induced by cavity collapse affect the detonation initiation process is still not fully understood. In this work, two-dimensional simulations are conducted for heterogeneous LX-17 energetic material containing array-distributed cavities to investigate the detonation initiation process induced by the impaction of the incident shock wave (ISW), and the impacts of cavity size and volume fraction on the shock-to-detonation transition (SDT) are also evaluated. First, we fix the cavity radius to be $40\ \mu\text{m}$ and the cavity volume fraction to be 12.57%, and compare the detonation initiation processes for neat and heterogeneous LX-17 energetic materials. The results indicate that cavities within LX-17 can accelerate the detonation initiation, i.e., shortening the initiation distance and time. Then, the flow characteristics and incident shock wave evolutions during the cavity collapse process are analyzed. The results show that the interaction between the cavity and the incident shock wave results in the local hot spots and causes LX-17 reactant to auto-ignite, so as to accelerate the shock-to-detonation transition. Finally, the influence of the cavity size and volume fraction on the detonation initiation process is assessed. It is found that as the cavity volume fraction increases, the detonation initiation distance and time increase and even become larger than the results predicted of the neat case, i.e., the acceleration effect of cavities on the detonation initiation weakens and the cavities even inhibits the shock-to-detonation transition. When the cavity volume fraction is fixed, it is found cases of small-size cavity predict longer initiation distance and time than cases of large-size cavity. The analysis indicates that increasing cavity volume fraction corresponds to smaller density of LX-17 reactant, and the hot spot duration time is shorter for cases of small-size cavity than cases of large-size cavity. Therefore, the detonation initiation distance and time increase as the cavity volume fraction increases and the cavity size decreases.

Published under an exclusive license by AIP Publishing. <https://doi.org/10.1063/5.0174851>

I. INTRODUCTION

During the manufacturing of energetic materials, imperfections may occur, such as air bubbles or foreign particles, leading to internal cavities and defects.^{1,2} The internal structure of heterogeneous energetic materials has a significant impact on their performance.^{3–6} Energetic materials, including explosives, propellants, and pyrotechnics, release energy through chemical reactions. The cavity in heterogeneous energetic material can impact its behaviors under shock waves, thus influencing crucial properties such as burn rate, pressure, and temperature and result in decreased performance and uneven burning.^{7,8} Hence, comprehending how internal cavity structure affects the

flow and reaction plays a critical role in the design and optimization of heterogeneous energetic materials.

Early studies focused on analyzing the flow evolutions during a single cavity collapse process induced by the impaction of the incident shock wave and the effects of chemical reactions were usually ignored.^{9,10} The results revealed that the jet induced by the cavity collapse played a critical role in local temperature rise, i.e., hot spot formation. Then, the influence of key factors such as the cavity shape and the angle between the incident shock wave and the non-circular cavity on hot spot formation was further studied.^{11–13} Recently, Michael *et al.*^{14,15} employed a high-precision numerical procedure to characterize the

wave structures during the cavity collapse process for nitromethane separately under reactive and non-reactive conditions. They numerically resolved the detailed flow characteristics resulting from the interaction between the incident shock wave and air–nitromethane interface. The effects of cavity collapse on temperature growth rates were quantized.¹⁵ In addition, the collapse process of multiple cavities impacted by an incident shock wave was also investigated,^{16–18} and the results indicated that interaction among waves induced by adjacent cavities could increase the local pressure peaks so as to affect the formation of hot spots.¹⁷

Although the cavity collapse induced by the incident shock wave can lead to hot spots formation and significantly affects the local temperature in heterogeneous energetic material, the effects of shock-induced cavity collapse on the full detonation initiation process, i.e., shock-to-detonation transition (SDT), have only recently become feasible to be evaluated due to advances in computing resources and programs.^{19–21} Mi *et al.*¹⁹ numerically observed the SDT process for liquid nitromethane filled with air cavities. They found air cavities within nitromethane could accelerate the strong incident shock wave develop to the detonation wave but prevent the SDT when the shock wave is weak.¹⁹ The impacts of cavity distributions on the detonation initiation process were also assessed, and the interaction among cavities was considered crucial for the SDT process.²⁰ In addition, Rai *et al.*²¹ employed an image-based level-set representation method to obtain the actual mesoscale structure of the cavity in a solid heterogeneous energetic material and evaluated how the irregular cavities affect the detonation initiation and propagation process. The results revealed that microstructures significantly impacted the ignition behavior of the energetic materials, emphasizing the critical role of microstructural details, such as void size, distribution, and orientation in the detonation initiation process.

In summary, cavities within heterogeneous energetic materials collapse when impacted by the incident shock wave and then induce hot spots. The mechanism of hot spot generation is well-understood, i.e., the interaction among density interfaces and shock waves during cavity collapse leads to the local temperature increasing (the formation of hot spots). However, how these hot spots affect the subsequent detonation initiation process has not been well studied and it is still not clear whether hot spots under different conditions accelerate detonation initiation. It is necessary to understand how some key factors, such as the cavity volume fraction and size, affect shock-to-detonation transition, which motivates the present work.

The present work aims to study how cavities within heterogeneous energetic material affect the detonation initiation process under the impact of an incident shock wave, i.e., the shock-to-detonation transition. As a composite material consisting of a fuel and an oxidizer, LX-17 has high energy density and is attractive for use in high-performance propulsion systems.^{22,23} In this work, two-dimensional numerical simulations on the scale of detonation induction length are

conducted for heterogeneous LX-17 containing cavities. It is assumed that the circular cavities within the LX-17 arrange in regular arrays. The detonation initiation processes for neat LX-17 (no cavities included) and heterogeneous LX-17 energetic material impacted by the same incident shock wave are compared at first. Then, the flow characteristics and shock wave evolutions are analyzed to show how cavity collapse accelerates the LX-17 react. Finally, the influence of cavity volume fraction and size on the shock-to-detonation transition is evaluated.

The paper is organized as follows. The model and numerical methods are introduced in Sec. II. Then, the shock-to-detonation transition for heterogeneous LX-17 containing cavities is simulated and discussed in Sec. III. The conclusions are summarized in Sec. IV.

II. NUMERICAL MODEL AND METHODS

The simulation domain is depicted in Fig. 1 and covers a rectangular region with length L and width H . The left boundary is set to zero-gradient, while the right boundary is modeled as a supersonic outlet. The top and bottom boundaries are set to cyclical. Region I ($x < 0.1$ mm) is filled with high-pressure LX-17 product (LX-17P) to generate the incident shock wave. Atmospheric LX-17 reactant (LX-17R) covers region II ($x > 0.1$ mm), while circular cavities covering region III are regularly arranged within LX-17 reactant. The cavity radius is denoted as r , and the distance between adjacent cavities is defined as δ . Regions II and III consist of square cells containing a single cavity arranging side by side, and the volume fraction of the cavity, V_C , is defined as

$$V_C = \frac{\pi r^2}{\delta^2}. \tag{1}$$

In the simulations, H is set to δ and L equals to 15 mm. The initial field is assumed to be stationary and other values at $t = 0$ are set to

$$(p, \rho, y_r, y_p, y_a) = \begin{cases} (21 \text{ GPa}, 2505 \text{ kg/m}^3, 0, 1, 0), & (x, y) \in \text{I} \\ (10^{-6} \text{ GPa}, 1905 \text{ kg/m}^3, 1, 0, 0), & (x, y) \in \text{II} \\ (10^{-6} \text{ GPa}, 1.25 \text{ kg/m}^3, 0, 0, 1), & (x, y) \in \text{III}, \end{cases} \tag{2}$$

where ρ is density and p is pressure of the mixture. y_r , y_p , and y_a are mass fractions of LX-17R, LX-17P, and air, respectively, and the sum of y_r , y_p , and y_a equals to unity.

The Euler equations developed based on four-equation model are used to describe the flow evolutions. Air, LX-17 reactant, and LX-17 product are assumed to be isothermal and isobaric. The governing equations are

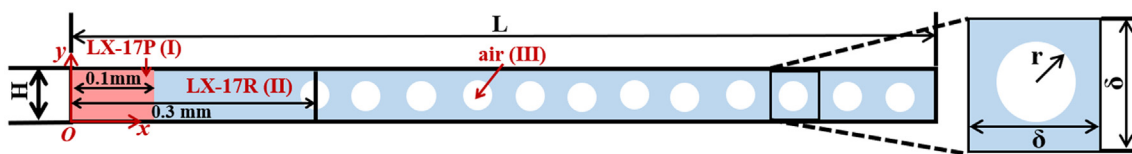


FIG. 1. Schematic of the simulation domain and initial settings.

TABLE I. Coefficients of the JWL equation for LX-17 reactant and product.

	ρ_0 (kg/m ³)	A_i (GPa)	B_i (GPa)	$R_{1,i}$	$R_{2,i}$	Cv_i (Pa/K)	ω_i	Q (GPa)
LX-17R	1905	77 810	-5.031	11.3	1.13	2.487×10^6	0.8938	6.9
LX-17P	1905	1481.05	63.79	6.2	2.2	1.0×10^6	0.5	0

$$\begin{aligned}
 \frac{\partial \rho}{\partial t} + \nabla \cdot (\rho V) &= 0 \\
 \frac{\partial(\rho V)}{\partial t} + \nabla \cdot (\rho VV) &= -\nabla p \\
 \frac{\partial(\rho E)}{\partial t} + \nabla \cdot [(\rho E + p)V] &= 0 \\
 \frac{\partial(\rho y_a)}{\partial t} + \nabla \cdot (\rho V y_a) &= 0 \\
 \frac{\partial(\rho y_p)}{\partial t} + \nabla \cdot (\rho V y_p) &= K,
 \end{aligned}
 \tag{3}$$

where $V = (u, v)$ is the velocity vector and E is the total energy. K is the source term caused by chemical reactions. Rai *et al.*'s work¹¹ has indicated that the contribution of cavity collapse induced by jet flow to the generation of hot spots significantly surpasses the frictional heating and adiabatic shear banding. Hence, the stress terms are ignored in Eq. (3). Similar simplifications are also employed in Refs. 4, 9, 24 The air is modeled as the ideal gas. The Mie–Grüneisen equation²⁴ is used to characterize the states of LX-17 reactant and product as

$$p_i = p_{\text{ref},i} + \omega_i \rho_i (e_i - e_{\text{ref},i}), \tag{4}$$

where i represents the type of the species, either the reactant ($i = r$) and the product ($i = p$). e_i is the internal energy, and ρ_i is the phase density. p_i is the phase pressure and $p_r = p_p = p$. ω_i is the Grüneisen coefficient. The reference pressure and reference internal energy for the LX-17 reactant and product are denoted as $p_{\text{ref},i}$ and $e_{\text{ref},i}$ respectively. Specifically, $p_{\text{ref},i}$ and $e_{\text{ref},i}$ are calculated using the Jones–Wilkins–Lee (JWL) equations^{25–27} as

$$\begin{aligned}
 p_{\text{ref},i} &= A_i \exp\left(\frac{-R_{1,i}\rho_0}{\rho_i}\right) + B_i \exp\left(\frac{-R_{2,i}\rho_0}{\rho_i}\right) \\
 e_{\text{ref},i} &= \frac{A_i}{\rho_0 R_{1,i}} \exp\left(\frac{-R_{1,i}\rho_0}{\rho_i}\right) + \frac{B_i}{\rho_0 R_{2,i}} \exp\left(\frac{-R_{2,i}\rho_0}{\rho_i}\right),
 \end{aligned}
 \tag{5}$$

where A_i , B_i , $R_{1,i}$, and $R_{2,i}$ are the coefficients calibrated according to the experimental data. ρ_0 is the reference density. Values of these coefficients are referred to^{26,28} and listed in Table I. In addition, Cv_i in Table I is the heat capacity, and Q is the calorific value of the LX-17 reactant.

TABLE II. Coefficients of Lee–Traver ignition and reaction model for LX-17 reactant.

I (s ⁻¹)	a	b	c	d	e	g	m
4.0×10^{12}	0.22	0.667	0.667	1.0	0.667	0.67	7.0
n	z	$\lambda_{\text{ig,max}}$	$\lambda_{G1,\text{max}}$	$\lambda_{G2,\text{min}}$	$G_1[(10^{11} \text{ Pa})^{-n} \text{ s}^{-1}]$	$G_2[(10^{11} \text{ Pa})^{-z} \text{ s}^{-1}]$	
3.0	1.0	0.02	0.8	0.8	4500×10^6	30×10^6	

The Lee–Traver ignition and reaction model [see Eq. (6)],²⁹ which has been widely used to characterize the ignition and reaction process for energetic materials, is employed to calculate the reaction rate as

$$\begin{aligned}
 \frac{d(1-\lambda)}{dt} &= -K = I(1-\lambda)^b (\rho/\rho_0 - 1 - a)^m \Psi(\lambda_{\text{ig,max}} - \lambda) \\
 &\quad + G_1(1-\lambda)^c \lambda^d p^n \Psi(\lambda_{G1,\text{max}} - \lambda) \\
 &\quad + G_2(1-\lambda)^e \lambda^g p^z \Psi(\lambda - \lambda_{G2,\text{min}}),
 \end{aligned}
 \tag{6}$$

where G_1 , G_2 , I , a , b , c , d , e , g , m , n , z , $\lambda_{\text{ig,max}}$, $\lambda_{G1,\text{max}}$, and $\lambda_{G2,\text{min}}$ are the coefficients calibrated according to experimental data. λ is the reaction process variable, and $\lambda = y_p/(y_r + y_p)$. Ψ is the Heaviside function. For LX-17 reactant, the coefficients in Eq. (6) are referred to^{26,28} and listed in Table II.

The in-house code, MEMD (multiphase energetic material detonation), is developed to solve the governing equations. MEMD uses the finite volume method. The second-order steepness-adjustable harmonic (SAH) scheme^{30,31} is employed for reconstruction, and the Harten-Lax-van Leer-contact (HLLC) approximate Riemann solver³² is used to calculate the convection fluxes. The third-order Runge–Kutta scheme is employed for time integration. To ensure the results in this work are reliable, the grid independence test and the program verification are conducted in Appendix A and Appendix B, respectively. For the simulations in Sec. III, uniform grids with $\delta x = \delta y = 0.39 \mu\text{m}$ are used.

III. RESULTS AND DISCUSSION

A. The detonation initiation for the neat/heterogeneous LX-17

The detonation initiation process initiated by the incident shock wave for the neat LX-17 is simulated at first. Figure 2 plots the temporal pressure distributions and reaction process variable distributions. It shows that the LX-17 reactant is compressed by the incident shock wave and its pressure increases from 10^{-6} GPa to 9.89 GPa at $t = 1 \mu\text{s}$, corresponding to the increased chemical reaction rate according to the Lee–Traver ignition and reaction model in Eq. (6). Subsequently, the compressed LX-17 reactant reacts and Fig. 2 indicates the reaction front moves from $x = 2.34 \text{ mm}$ at $t = 1 \mu\text{s}$ to $x = 4.44 \text{ mm}$ at $t = 1.2 \mu\text{s}$. At $t = 1 \mu\text{s}$, a significant pressure peak is observed near the reaction

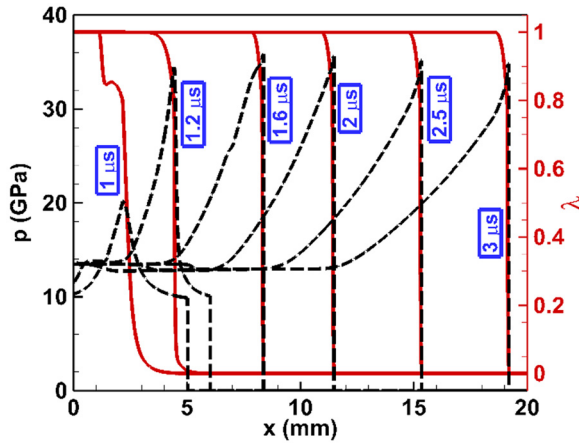


FIG. 2. Temporal pressure distributions (black lines) and reaction process variable distributions (red lines) during the detonation initiation process for the case of neat LX-17.

front, resulting from the convergence of pressure waves accompanying reactions. Then, the pressure peak couples with reaction front and converts to a detonation wave at $t = 1.2 \mu\text{s}$, as seen in Fig. 2. When $t > 2 \mu\text{s}$, the detonation wave has caught up with the incident shock wave and converts to a stable propagating detonation wave. The detonation wave propagation speed (S_D) and the pressure at Von-Neumann spike (P_{VN}) predicted in this work are 7691.3 m/s and 34.8 GPa, respectively, almost consistent with the results predicted by the Chapman–Jouguet (C–J) theory, i.e., 7679.9 m/s and 34.8 GPa.²⁸ This further confirms the reliability of numerical models and program used in this work.

Then, the detonation initiation process for heterogeneous LX-17 containing cavities is simulated. The cavity radius is set to $40 \mu\text{m}$ and δ equals to $200 \mu\text{m}$; i.e., the cavity volume fraction is 12.57% according to Eq. (1). Figure 3 displays the temporal density contours during the detonation initiation and propagation process. It shows that the wave front is periodically disturbed by cavities and becomes irregular. Qualitatively, as seen in Fig. 3, the density behind the wave front is highly uneven, causing varying reaction rates and impacting the detonation initiation process.

Since the wave front is inhomogeneous due to cavity interference during propagation, the average quantities along y direction are calculated to identify the position of the wave front. The average pressure and reaction process variable distributions in the y direction at different times are recorded in Fig. 4. Intense pressure oscillations behind

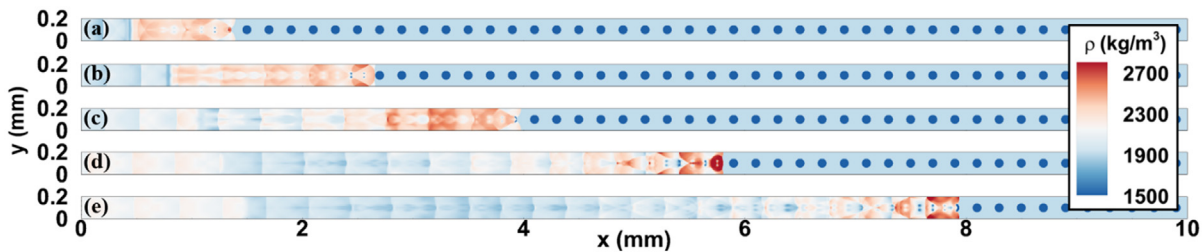


FIG. 3. Temporal density contours for heterogeneous LX-17 impacted by the incident shock wave. $V_C = 12.57\%$ and $r = 40 \mu\text{m}$. (a) $t = 0.3 \mu\text{s}$, (b) $t = 0.6 \mu\text{s}$, (c) $t = 0.9 \mu\text{s}$, (d) $t = 1.2 \mu\text{s}$, and (e) $t = 1.5 \mu\text{s}$.

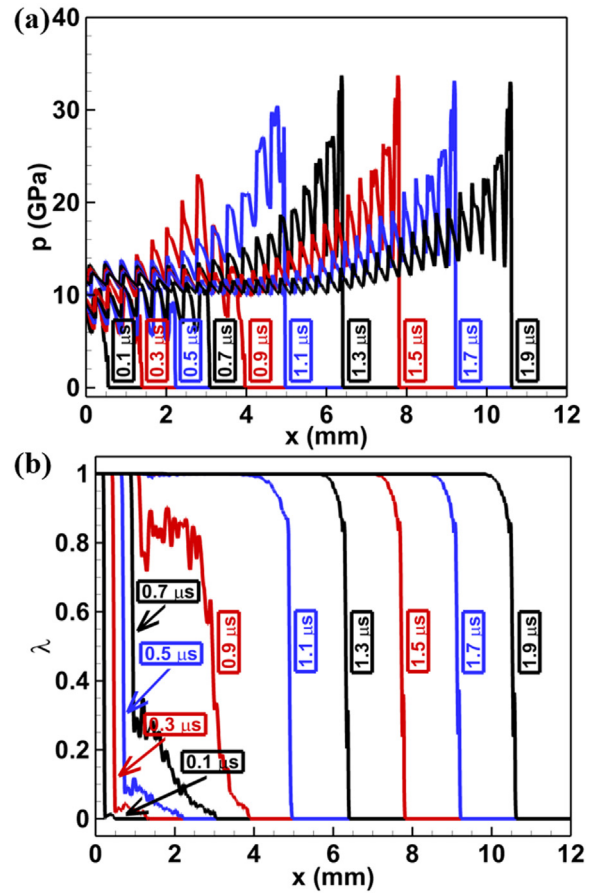


FIG. 4. Temporal (a) pressure and (b) reaction process variable distributions during the shock-to-detonation transition process for heterogeneous LX-17. $V_C = 12.57\%$ and $r = 40 \mu\text{m}$.

the incident shock wave, resulting from the periodic interruption of cavities to the wave front, are observed in Fig. 4. Ignoring the pressure and reaction process variable oscillations caused by the cavities, the detonation initiation process for heterogeneous LX-17 in Fig. 4 is similar to that for neat LX-17 shown in Fig. 2. Both the shock-to-detonation transition processes shown in Figs. 2 and 4 can be divided into three stages. First, the incident shock wave compresses the fresh LX-17 reactant, triggering initial reactions. Then, pressure waves converge to

form the shock-reaction structure, i.e., the temporary detonation wave. Finally, the shock-reaction front catches up with the incident shock wave, converting to the stable propagating detonation wave.

Pressure profiles for cases of neat LX-17 (as shown in Fig. 2) and heterogeneous LX-17 (as shown in Figs. 3 and 4) are presented in x - t diagrams in Fig. 5. The initiation distance, x_i , is denoted as the distance from the left inlet to the position reaction front catching up with the incident shock wave and the time consumed in this process is defined as the initiation time, t_i . For the case of neat LX-17, x_i equals to 7.4 mm and t_i equals to 1.51 μ s [as shown in Fig. 5(a)]. For the case of heterogeneous LX-17, x_i is 4.7 mm and t_i is 1.07 μ s [as shown in Fig. 5(b)]. Comparing with the case of neat LX-17, the initiation distance reduces by 36.5% and the initiation distance reduces by 29.1% for the case of heterogeneous LX-17, i.e., cavities significantly accelerate the shock-to-detonation transition.

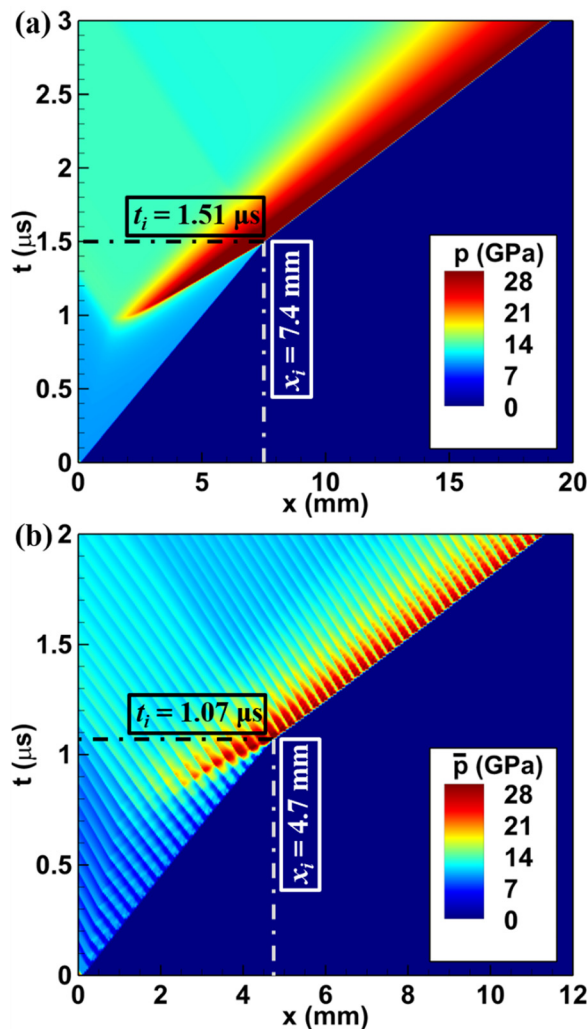


FIG. 5. x - t diagrams of pressure profiles for cases of (a) neat LX-17 (as shown in Fig. 2) and (b) heterogeneous LX-17 (as shown in Figs. 3 and 4).

To explain how cavities accelerate the detonation initiation, the probability density function (PDF), $f(q, x)$, for the case of heterogeneous LX-17 are plotted in Fig. 6. Here, q is the volumetric heat release rate. The maximum heat release rate for the case of neat LX-17, $q_{max, neat}$ is also signed with the black lines in Fig. 6 as the reference. Figures 6(a) and 6(b) show the heat release rate in part of the region behind the incident shock wave for heterogeneous case is significantly higher than the maximum exothermic rate of the neat case at $t = 0.6 \mu$ s and 0.9μ s. It indicates that cavities in heterogeneous LX-17 cause an increased exothermic rate of the reactant compared to the case of neat LX-17, resulting in the reactant ignites earlier so as to accelerate the detonation initiation process. At $t = 1.2 \mu$ s, the steady detonation wave has formed and it is seen in Fig. 6(c) that the exothermic rate in the region just behind the incident shock wave is remarkably high; i.e., LX-17 reactant reacts right away after compressed by the leading shock wave and the reaction front couples with the leading shock wave.

B. The formation mechanism of hot spots

To explain how cavities within heterogeneous LX-17 promote the reactant release heat and accelerate detonation initiation, we take the cavity at the first column as an example and analyze the wave evolutions when it is impacted by the incident shock wave (ISW). Figure 7 shows temporal density and pressure contours during the cavity collapse process. At $t = 31$ ns, it is seen in Fig. 7(a) that the incident shock wave has not touched the cavity yet. Then, at $t = 38$ ns [see Fig. 7(b)], the incident shock wave interacts with the left reactant-air interface (LRAI) and rarefaction waves (RW) are reflected upstream, causing lower pressure in the left region of the cavity. Then, the incoming flows toward the low-pressure region and converges at the center of the cavity [see the streamlines shown in Fig. 7(c) at $t = 50$ ns], resulting in a jet flow propagating along the line $y = 0.1$ mm. At $t = 60$ and 65 ns, as Figs. 7(d) and 7(e) show, the jet flow impacts on the right reactant-air

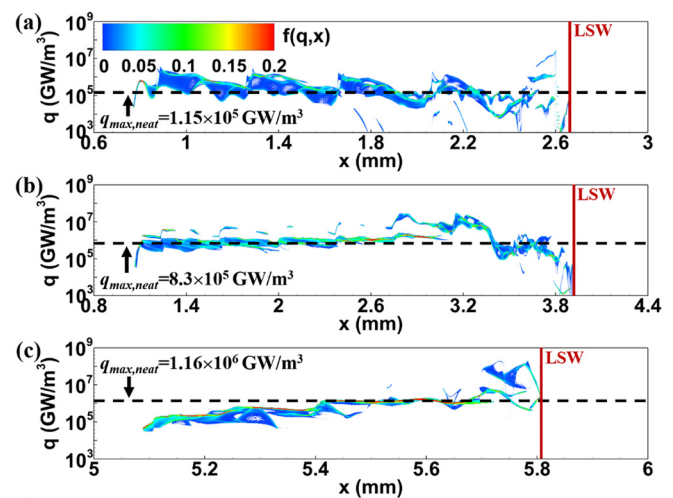


FIG. 6. Probability density function, $f(q, x)$, as a function of heat release rate, q , for the case of heterogeneous LX-17 during the shock-to-detonation transition process. The black dashed line is the maximum exothermic rate for the case of neat LX-17, and the red line represents the position of the leading shock wave (LSW) front. (a) $t = 0.6 \mu$ s, (b) $t = 0.9 \mu$ s, and (c) $t = 1.2 \mu$ s.

08 April 2024 03:49:53

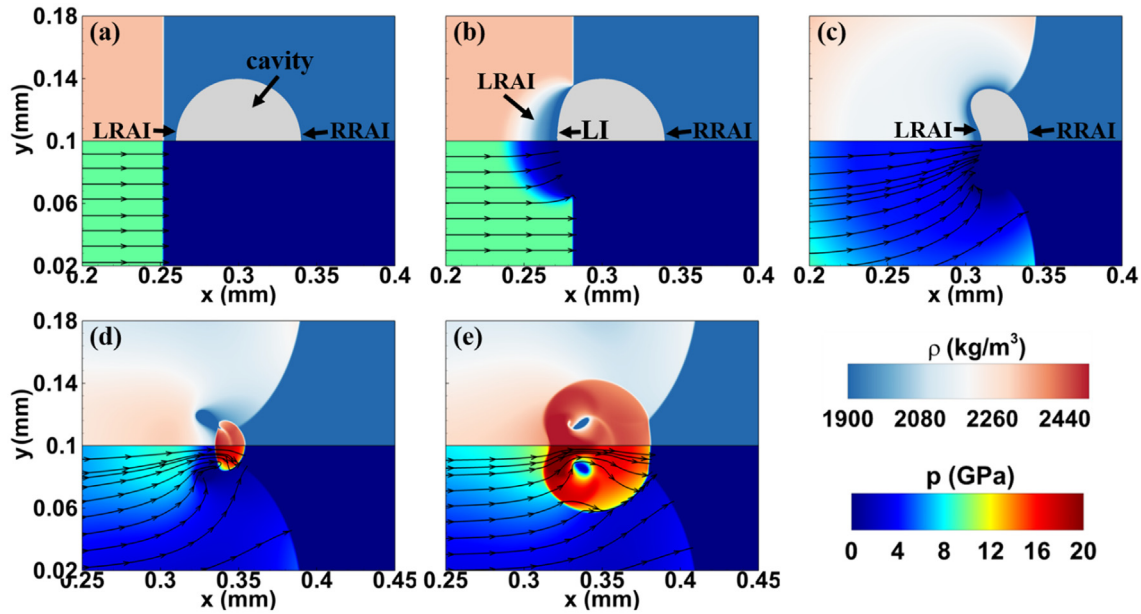


FIG. 7. Temporal density contours (upper) and pressure contours along with streamlines (lower) during cavity collapse process. (a) $t = 31$ ns, (b) $t = 38$ ns, (c) $t = 50$ ns, (d) $t = 60$ ns, and (e) $t = 65$ ns.

interface (RRAI), strongly compressing the surrounding LX-17 reactant and increasing local pressure and density. It is expected that the reaction rate in compressed regions increases according to Eq. (6) so as to promote LX-17 reactant ignite, i.e., inducing hot spots.

Figure 8 displays the wave structures and exothermic rate contours after the cavity collapses. At $t = 58$ ns, it is seen in Fig. 8(a) that the jet flow impacts the right air-reactant interface, forming a transmitted shock wave (TSW) and a reflected shock wave (RSW). In Figs. 8(b) and 8(d), the TSW and the RSW move upstream and

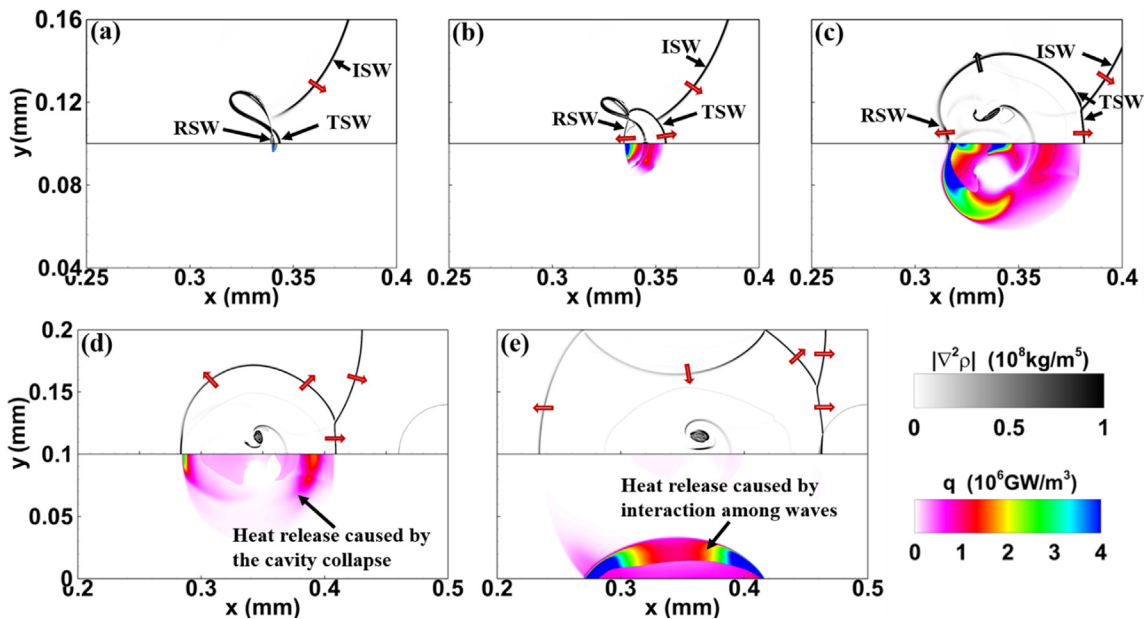


FIG. 8. Temporal numerical schlieren images (upper) and heat release contours (lower) during the cavity collapse process. The red arrows indicate the wave movement directions. (a) $t = 58$ ns, (b) $t = 60$ ns, (c) $t = 65$ ns, (d) $t = 70$ ns, and (e) $t = 80$ ns.

downstream, respectively, compressing the reactant and giving rise to high exothermic rates. It is seen in Fig. 8(e) that waves induced by adjacent cavities collide at $t = 80$ ns, compressing the reactant and inducing it release heat. Comparing the results in Figs. 8(c) and 8(e), it is noted that maximum exothermic rates in reaction regions separately induced by cavity collapse and wave collision are the same order of magnitude. It highlights that interactions among waves induced by adjacent cavities also play a significant role in hot spot formations, which is ignored in previous studies.

C. Impacts of cavity volume fraction and size on the detonation initiation

In Secs. III A and III B, we have compared the detonation initiation processes for neat LX-17 and heterogeneous LX-17, and the regime how cavity collapse within heterogeneous LX-17 induces the formation of hot spots and accelerates the shock-to-detonation transition is analyzed. Then, effects of cavity volume fraction and size on the detonation initiation process for heterogeneous LX-17 are assessed in this section. The settings for cases 1–9 are listed in Table III. Cases 1, 4, and 7 share the similar cavity distributions, i.e., $V_C = 6.28\%$ and $r/\delta = 0.1414$. For cases 2, 5, and 8, $V_C = 12.57\%$ and $r/\delta = 0.2$, while $V_C = 25.13\%$ and $r/\delta = 0.2828$ for cases 3, 6, and 9.

Figure 9 records the velocity of the leading shock wave, S , during the detonation initiation and propagation processes for cases 1–9. In Fig. 9(a), for cases 1, 4, and 7, the propagation speeds of successfully initiated detonation waves equal to 7265 m/s, 7272 m/s, and 7321 m/s, respectively. For cases 2, 5, and 8 shown in Fig. 9(b), the detonation propagation speeds are 6996 m/s, 6992 m/s, and 7033 m/s, respectively. For cases 3, 6, and 9, it is seen in Fig. 9(c) that the detonation propagation speeds are 6528 m/s, 6521 m/s, and 6548 m/s, respectively. The results suggest that the detonation propagation speeds are almost consistent when the cavity volume fraction is fixed. According to the C–J theory, the detonation wave propagation speed is determined by the heat release. When the cavity volume fraction is fixed, the average heat release per unit volume remains constant, resulting in almost unchanged detonation wave propagation speed.

The initiation times and distances of detonation initiation processes shown in Fig. 9 are counted in Fig. 10. It is observed that initiation time and distance decrease with the cavity radius increases when the cavity volume fraction keeps constant. Taking cases that V_C equals to 12.57% as instances, Fig. 10 shows that $t_i = 1.50 \mu\text{s}$, $1.08 \mu\text{s}$, and

TABLE III. Settings of cavity size and volume fraction for cases 1–9.

	δ (μm)	r (μm)	V_C (%)	r/δ
Case 1	400	56.57	6.28	0.1414
Case 2	400	80	12.57	0.2
Case 3	400	113.14	25.13	0.2828
Case 4	200	28.28	6.28	0.1414
Case 5	200	40	12.57	0.2
Case 6	200	56.57	25.13	0.2828
Case 7	100	14.14	6.28	0.1414
Case 8	100	20	12.57	0.2
Case 9	100	28.28	25.13	0.2828

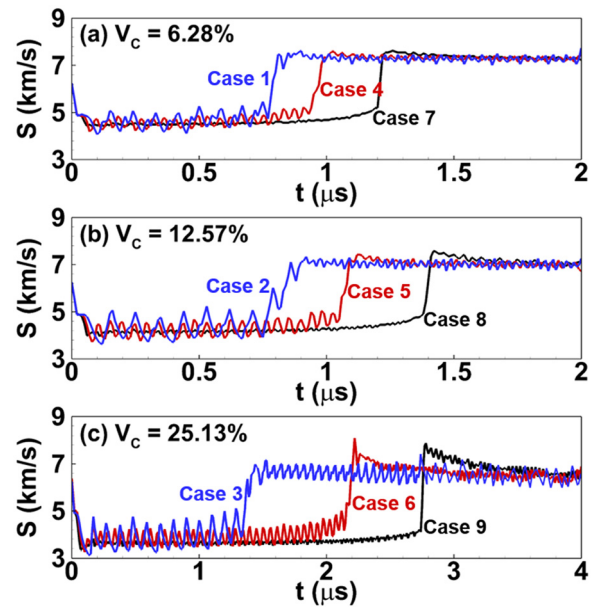


FIG. 9. The leading shock wave speeds vary with time during detonation initiation processes for heterogeneous LX-17 of cases 1–9. (a) $V_C = 6.28\%$, (b) $V_C = 12.57\%$, and (c) $V_C = 25.13\%$.

$0.78 \mu\text{s}$, $x_i = 6.12$, 4.84 , and 3.52 mm for cases of $r = 20 \mu\text{m}$, $40 \mu\text{m}$, and $80 \mu\text{m}$, respectively. When δ is fixed to $200 \mu\text{m}$ (cases 4, 5, and 6), as the cavity volume fraction increases from 6.28% to 12.57% and then to 25.13%, the corresponding initiation time increases from $0.98 \mu\text{s}$ to $1.08 \mu\text{s}$ and then to $2.15 \mu\text{s}$, and the initiation distance increases from 4.71 mm to 4.84 mm and then to 8.39 mm. However, $t_i = 0.78 \mu\text{s}$ and

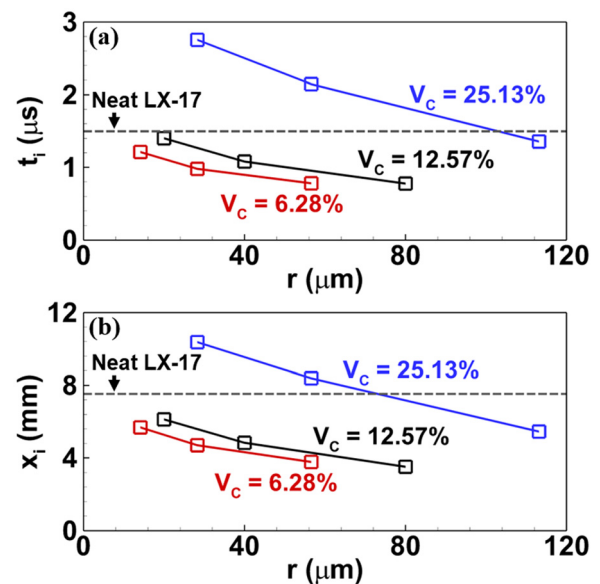


FIG. 10. The detonation (a) initiation times and (b) initiation distances for the case of neat LX-17 and cases 1–9 of heterogeneous LX-17.

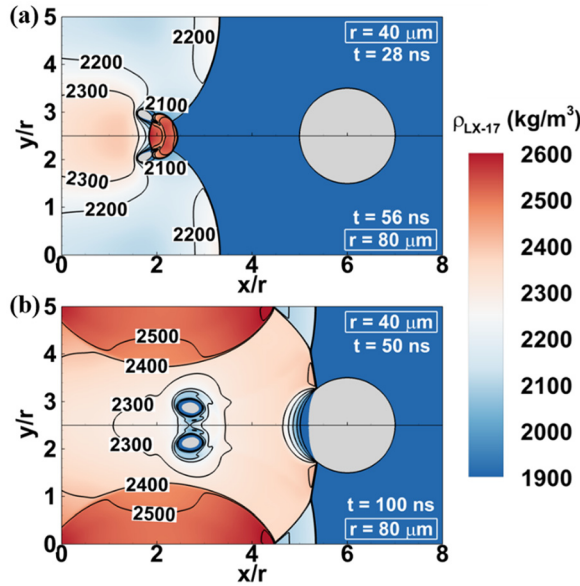


FIG. 11. Temporal density contours during the first cavity collapse process for case 2 (lower) and case 5 (upper) in dimensionless coordinates. (a) $t = 28$ ns for case 5 and $t = 56$ ns for case 2, (b) $t = 50$ ns for case 5, and $t = 100$ ns for case 2.

$x_i = 3.78$ mm for case 1 ($\delta = 400 \mu\text{m}$ and $V_C = 6.28\%$), while $t_i = 0.77 \mu\text{s}$ and $x_i = 3.52$ mm case 2 ($\delta = 400 \mu\text{m}$ and $V_C = 12.57\%$), i.e., both the initiation time and distance decrease as the cavity volume fraction increases, showing an opposite trend with the cases $\delta = 200 \mu\text{m}$. In addition, $t_i = 2.14 \mu\text{s}$ and $x_i = 8.38$ mm for case 6 ($\delta = 200 \mu\text{m}$ and $V_C = 25.13\%$), while $t_i = 2.75 \mu\text{s}$ and $x_i = 10.33$ mm for case 9 ($\delta = 100 \mu\text{m}$ and $V_C = 25.13\%$). Both detonation initiation distances and times of these two cases are larger than the results of neat LX-17

($t_i = 1.51 \mu\text{s}$ and $x_i = 7.4$ mm), i.e., cavities within heterogeneous LX-17 for cases 6 and 9 inhibit the shock-to-detonation transitions.

The results shown in Fig. 10 highlight two issues. The first one is that the SDT is more significantly accelerated for cases of larger cavities than cases of smaller cavities when the cavity volume fraction is fixed. The second one is that the SDT is inhibited when the cavity volume fraction is large and the cavity size is small. These two issues are explained below.

Temporal density contours during the first cavity collapse process for case 2 ($\delta = 400 \mu\text{m}$, $r = 80 \mu\text{m}$, and $V_C = 12.57\%$) and case 5 ($\delta = 200 \mu\text{m}$, $r = 40 \mu\text{m}$, and $V_C = 12.57\%$) are illustrated in dimensionless coordinates in Fig. 11. The cavity radius is set as the reference length and the coordinate origin locates at the point $x = 0.22$ mm and $y = 0.2$ mm for case 2 while at the point $x = 0.26$ mm and $y = 0.1$ mm for case 5. It is seen in Fig. 11(a) that the density distribution at $t = 28$ ns for case 5 is almost consistent with that at $t = 56$ ns for case 2. The similarity of flow structures is further verified in Fig. 11(b) where density distributions for case 5 at $t = 50$ ns and case 2 at $t = 100$ ns are plotted. Using r/u_0 (u_0 is the inflow velocity) as the reference time, flow structures of case 2 and case 5 shown in dimensionless space and time coordinates are similar. The similarity of the flow structures between case 2 and case 5 is employed to explain why detonation initiation distances and times for cases of larger cavities are smaller than results for cases of smaller cavities as follows.

In Fig. 12, we mark the reactant in the first square cell and track its density distribution over time. It is observed in Fig. 12(a) that part of the LX-17 reactant is compressed and its density is significantly higher than others after the cavity collapses. The jet induced by cavity collapse develops, forming the spike structure as shown in Figs. 12(b)–12(e). In addition, it is also seen that when the downstream cavities collapse, the upstream propagating shock waves induced by collapse of these cavities further compress the marked LX-17 reactant and increase its density.

The PDF of the marked reactant density, $f(\rho, t)$, is plotted in Fig. 13. It is seen that the reactant density increases since the local

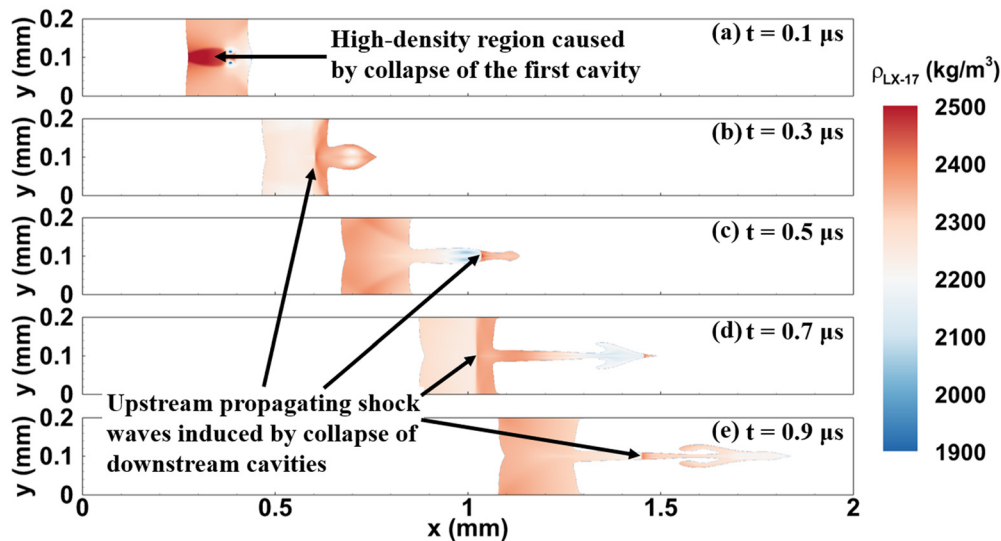


FIG. 12. Temporal density distributions of LX-17 reactant in the first square cell for case 5. (a) $t = 0.1 \mu\text{s}$, (b) $t = 0.3 \mu\text{s}$, (c) $t = 0.5 \mu\text{s}$, (d) $t = 0.7 \mu\text{s}$, and (e) $t = 0.9 \mu\text{s}$.

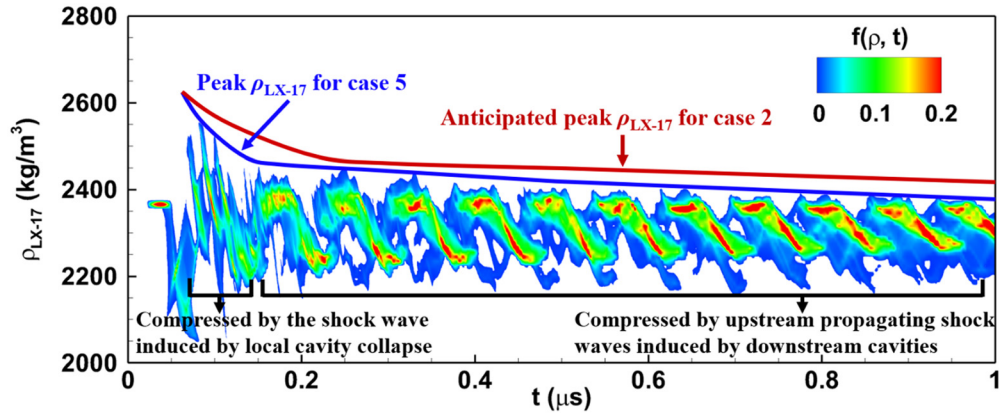


FIG. 13. The temporal PDF of the marked LX-17 reactant density, $f(\rho, t)$, for case 5. The blue line is the fitted peak density evolutions for case 5, and the red line is the predicted peak density evolutions for case 2 according to the flow similarity between case 2 and case 5.

cavity collapses at first. Then, the upstream propagating shock waves induced by collapse of downstream cavities compress the reactant and frequently increase its density. As the leading shock wave propagates downstream, waves induced by downstream cavities become weaker when it reaches to the marked reactant, resulting in weaker compression effects. In Fig. 13, we fit the peak density of the marked reactant with blue line and it shows that the peak density decreases with time. According to the flow similarity between case 2 and case 5 as shown in Fig. 11, i.e., the flow state for case 5 at time $t = t_1$ is approximately similar to that for case 2 at $t = 2t_1$, the red line representing the temporal peak density of the reactant in the first square cell for case 2 is anticipated and plotted in Fig. 13. The results indicate that the peak density for case 2 ($r = 80 \mu\text{m}$) decays more slowly compared with that for case 5 ($r = 40 \mu\text{m}$), i.e., intensity of hot spots induced by cavity collapse decreases more rapidly for cases of heterogeneous LX-17 containing smaller cavities. Therefore, initiation time and distance decrease with the cavity radius increasing when the cavity volume fraction is fixed, as illustrated in Fig. 10.

Although the results in Sec. III B indicate that cavity collapse results in the formation of hot spots and reactant ignition, the detonation initiation processes are inhibited for case 6 and case 9 when the cavity volume fraction is large enough. To explain this point, the temporal density PDF of reactant compressed by the incident shock wave at $t = 0.6 \mu\text{s}$ for case 4 ($\delta = 200 \mu\text{m}$ and $V_C = 6.28\%$), case 5 ($\delta = 200 \mu\text{m}$ and $V_C = 12.57\%$), and case 6 ($\delta = 200 \mu\text{m}$ and $V_C = 25.13\%$) is counted in Fig. 14. It is seen that there are two PDF peaks of the LX-17 reactant for all three cases. The first peak corresponds to the compressed reactants far away from cavities, whose value closed to the compressed reactant density of the neat case, i.e., 2409 kg/m^3 . When the cavity collapses, LX-17 reactants surrounding it fill the space, resulting in the density of nearby reactants decrease. As the cavity volume fraction increases, more reactants fill the cavity space and reactant density behind the incident shock wave reduces to lower values. As expected, the second PDF peaks in Figs. 14(a)–14(c) corresponding to reactants surrounding cavities for case 4 ($V_C = 6.28\%$), case 5 ($V_C = 12.57\%$), and case 6 ($V_C = 25.13\%$), equal to 2343.3 kg/m^3 , 2302.5 kg/m^3 , and 2230.7 kg/m^3 , respectively. As a result, the reaction rate decreases, while the detonation initiation

distance and time increase as the cavity volume fraction increases. When the cavity volume fraction is large enough, the shock-to-detonation transition is inhibited.

In summary, the cavity collapse causes local reactants are greatly compressed within a short period of time, inducing formation of hot spots and accelerating the detonation initiation. However, reactants surrounding the cavity fill the void and the density of these reactants decreases, resulting in the decreasing reaction rate and inhibiting the shock-to-detonation transition. Hence, when the cavity volume fraction is large enough, both the detonation initiation distance and time for cases of heterogeneous LX-17 are larger than the results predicted by the case of neat LX-17 (see case 6 and case 9 in Fig. 10); i.e., the

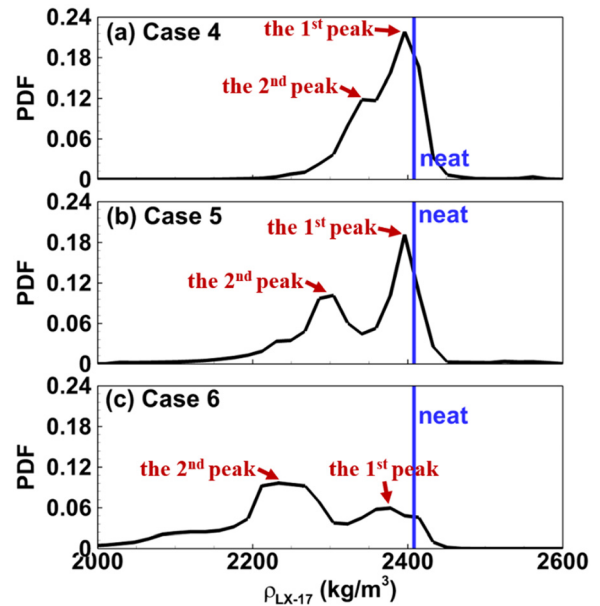


FIG. 14. The density PDF of reactants compressed by the incident shock wave at $t = 0.6 \mu\text{s}$ for (a) case 4 ($\delta = 200 \mu\text{m}$ and $V_C = 6.28\%$), (b) case 5 ($\delta = 200 \mu\text{m}$ and $V_C = 12.57\%$), and (c) case 6 ($\delta = 200 \mu\text{m}$ and $V_C = 25.13\%$).

detonation initiation process is inhibited. In contrast, when the cavity size is large and the cavity volume fraction is small, the detonation initiation processes are significantly accelerated, as cases 1–3 in Fig. 10 show.

IV. CONCLUSIONS

This work simulates the detonation initiation processes in a heterogeneous LX-17 energetic material impacted by an incident shock wave. The objective is to understand how cavities within LX-17 reactant affect the detonation initiation. The mechanism of hot spot formation induced by cavity collapse is interpreted. Moreover, the effects of cavity size and volume fraction on the shock-to-detonation transition are assessed.

First, we compare detonation initiation processes between the case of heterogeneous LX-17 ($r = 40 \mu\text{m}$ and $\delta = 200 \mu\text{m}$) and the case of neat LX-17. Compared with results of the neat case, the detonation initiation distance and time for the heterogeneous case are reduced by 29.1% and 36.5%, respectively. The hot spot formation is found to play a critical role in accelerating the shock-to-detonation transition. Then, the flow characteristics and shock wave dynamics during the cavity collapse are analyzed. The results indicate that the jet flow induced by the cavity collapse impacts on the air-reactant interface and compresses the LX-17 reactant, resulting in the early ignition of the reactant, i.e., forming the hot spots. In addition, the present results highlight that interactions among waves induced by adjacent cavities are also critical in hot spot formations, which is usually ignored in previous studies. Finally, detonation initiation processes for heterogeneous LX-17 of different cavity volume fractions and sizes are simulated. When the cavity volume fraction is fixed, the detonation initiation distance and time for cases of large cavities are smaller than those for cases of small cavities, resulting from the slower decay rate of the hot spot intensity according to the flow similarity analysis. As the cavity volume fraction increases, more reactants surrounding cavities fill the void after cavities collapse and densities of these reactants decrease, resulting in the decreasing reaction rate and increasing detonation initiation distance and time. However, when the cavity volume fraction is large enough and the cavity size is small enough, the detonation initiation process is inhibited.

Note that the cavity radius considered in this work is much smaller than the detonation initiation distance; i.e., the detonation wave cannot be induced by collapses of few cavities. When the cavity radius is large so that the detonation wave forms during the single cavity collapse, conclusions drawn from this work are not applicable. In addition, cylindrical cavities are assumed to be regularly arranged within LX-17 material in this work. Although there is different from the practical situation, these simplifications help to essentially explain the mechanisms how the cavity size and volume fraction affect the shock-to-detonation transition. In future studies, more realistic cavity shape and distribution should be considered.

ACKNOWLEDGMENTS

This work was supported by the National Natural Science Foundation of China (Nos. 12002063 and 12202014) and the National Key Project of China (No. GJXM92579). We thank Drs. Yupei Qin, Haifeng Li from Institute of Applied Physics and Computational Mathematics in China for helping to develop the MEMD program.

AUTHOR DECLARATIONS

Conflict of Interest

The authors have no conflicts to disclose.

Author Contributions

Jie Sun: Formal analysis (lead); Methodology (lead); Software (equal); Writing – original draft (lead). **Pengfei Yang:** Writing – review & editing (equal). **Baoqing Meng:** Funding acquisition (lead); Software (lead); Writing – review & editing (equal). **Rui Zhou:** Conceptualization (supporting); Software (supporting). **Baolin Tian:** Methodology (lead); Software (lead); Writing – review & editing (equal). **Zheng Chen:** Formal analysis (equal); Methodology (equal); Writing – review & editing (lead).

DATA AVAILABILITY

The data that support the findings of this study are available from the corresponding author upon reasonable request.

APPENDIX A: GRID INDEPENDENCE TESTS

To demonstrate the results presented in this work are independent of grids, detonation initiation processes with grid sizes of $0.78 \mu\text{m}$, $0.39 \mu\text{m}$, and $0.20 \mu\text{m}$ are simulated. The cavity volume fraction is fixed to 12.57%, and the cavity radius equals to $40 \mu\text{m}$. Figure 15(a) shows the density contours are almost consistent for cases of grid sizes equaling to $0.39 \mu\text{m}$ and $0.20 \mu\text{m}$. The leading shock wave speeds during detonation initiation processes for these three cases are recorded in Fig. 15(b). Detonation initiation times

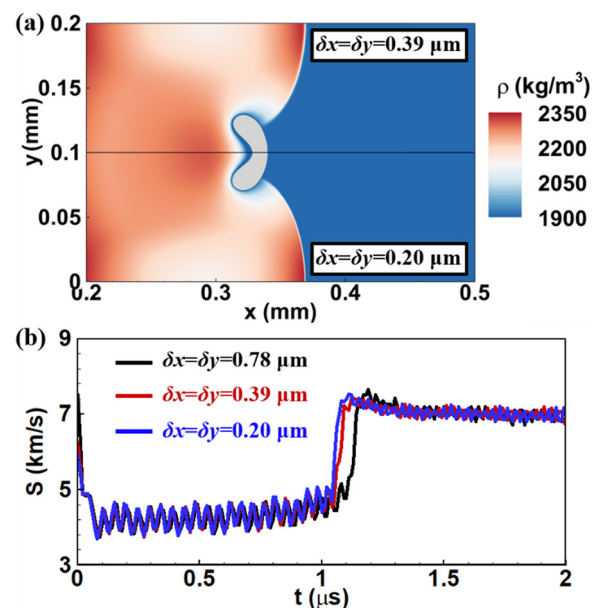


FIG. 15. Comparison of results predicted by cases of grid sizes equaling to $0.78 \mu\text{m}$, $0.39 \mu\text{m}$, and $0.20 \mu\text{m}$. $V_C = 12.57\%$ and $r = 40 \mu\text{m}$. (a) Density contours at $t = 55 \text{ ns}$ for cases of grid sizes equaling to $0.39 \mu\text{m}$ and $0.20 \mu\text{m}$ and (b) the leading shock wave speed varies with time for these three cases.

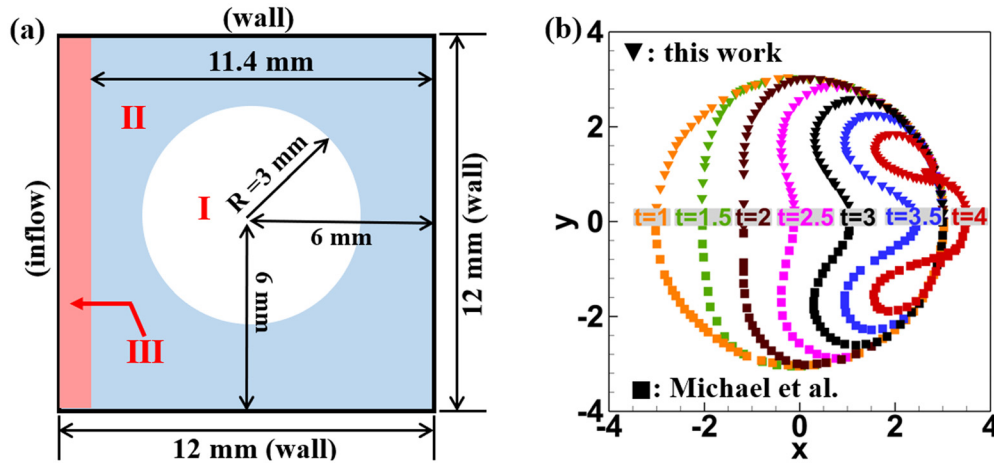


FIG. 16. The collapse process of an air bubble within water induced by an incident shock wave. (a) Schematic of the simulation settings and (b) the bubble shape evolutions predicted in this work and results provided by Michael *et al.*¹⁴ Note the results are dimensionless, and the reference values are same with Michael *et al.*'s work.¹⁴

for cases of grid sizes equaling to $0.78 \mu\text{m}$, $0.39 \mu\text{m}$, and $0.20 \mu\text{m}$ are $1.13 \mu\text{s}$, $1.07 \mu\text{s}$, and $1.05 \mu\text{s}$, respectively. Hence, uniform grids with size of $\delta x = \delta y = 0.39 \mu\text{m}$ are accurate enough to ensure the simulation results are independent of grids and used in this work.

APPENDIX B: CODE VALIDATION

In Sec. III A, we have compared the detonation wave velocity predicted by the in-house code MEMD with the result predicted by the C-J theory. To further valid the reliability of MEMD, the collapse process of an air bubble within water is simulated. Figure 16(a) shows the schematic of the simulation settings and the initial states are set as

$$\begin{aligned}
 & (p, \rho, u, v, y_{\text{water}}, y_{\text{air}}) \\
 & = \begin{cases} (10^{-6} \text{ Mbar}, 1.2 \text{ kg/m}^3, 0, 0, 0, 1) & (x, y) \in \text{I} \\ (10^{-6} \text{ Mbar}, 1000 \text{ kg/m}^3, 0, 0, 1, 0) & (x, y) \in \text{II} \\ (21 \text{ Mbar}, 1325 \text{ kg/m}^3, 680.5 \text{ m/s}, 0, 1, 0) & (x, y) \in \text{III}, \end{cases} \\
 & \hspace{15em} \text{(B1)}
 \end{aligned}$$

where $\rho, p, (u, v), y_{\text{water}}$, and y_{air} are the density, pressure, velocity vector, mass fraction of water, and mass fraction of air, respectively. Figure 16(b) records the bubble shape evolutions predicted by this work. The results show a good agreement with results provided by Michael *et al.*¹⁴ The reliability of the mathematical model and program used in this work is furtherly confirmed.

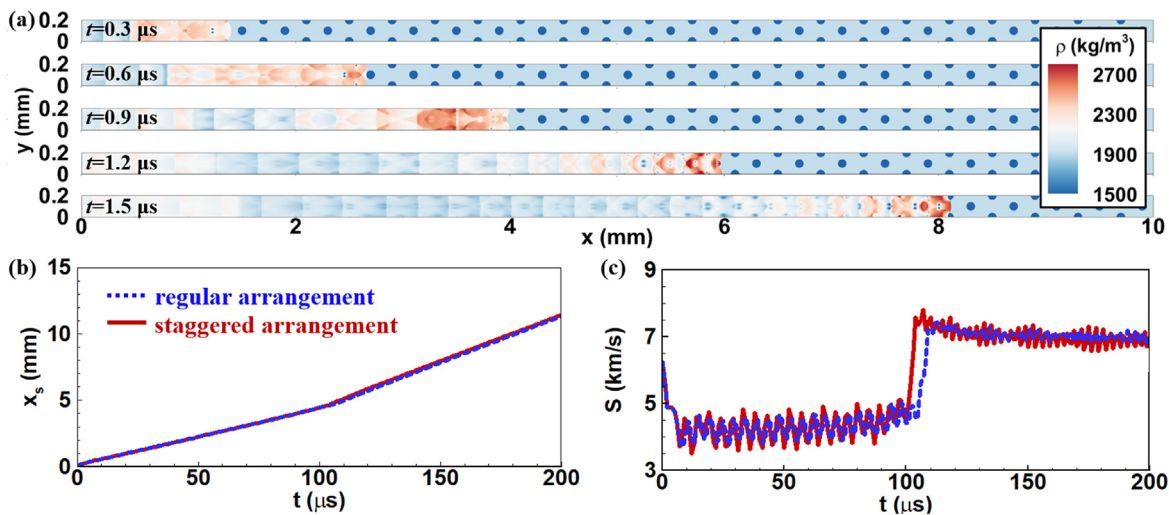


FIG. 17. Detonation initiation processes for heterogeneous LX-17 with staggered cavities impacted by the incident shock wave. $V_c = 12.57\%$ and $r = 40 \mu\text{m}$. (a) Temporal density contours, (b) position, x_s , and (c) propagation speed, S , of the leading shock waves vary with time for cases of staggered cavities and regular cavities.

APPENDIX C: THE INFLUENCE OF CAVITY ARRANGEMENT

The influence of cavity arrangement is evaluated in this appendix. Different from the regularly arranged cavities above, cavities are adjusted to staggered arrangement. The cavity volume fraction is set to 12.57%, and the cavity radius equals to 40 μm . Figure 17(a) displays the temporal density contours during the detonation initiation and propagation process for heterogeneous LX-17 containing staggered cavities, which is similar to the results shown in Fig. 3 predicted by the case of regularly arranged cavities. Positions (x_i) and propagation speeds (S) of the leading shock waves both for cases of staggered cavities and regular cavities are recorded in Figs. 17(b) and 17(c). Figure 17(b) illustrates temporal positions of the wave fronts are almost consistent for these two cases. As Fig. 17(c) shows, the detonation initiation times predicted by cases of staggered cavities and regular cavities are closed and equal to 1.04 μs and 1.07 μs , respectively.

The results in Figs. 3 and 17 indicate that the cavity configuration has little influence on the detonation process and initiation time. In addition, this work focuses on assessing the effects of cavity volume fraction and cavity radius on the shock-to-detonation transition. The influence of cavity arrangement on results is not the focus. Hence, cavities are set to regular arrangement. The effects of cavity arrangement on detonation initiation processes will be studied in future works.

REFERENCES

- A. Higgins, J. Loiseau, and X. C. Mi, "Detonation velocity/diameter relation in gelled explosive with inert inclusions," *AIP Conf. Proc.* **1979**, 100019 (2018).
- C. D. Yarrington, R. R. Wixom, and D. L. Damm, "Shock interactions with heterogeneous energetic materials," *J. Appl. Phys.* **123**, 105901 (2018).
- D. M. Dattelbaum, S. A. Sheffield, D. B. Stahl, and A. M. Dattelbaum, "Influence of hot spot features on the shock initiation of heterogeneous nitromethane," *AIP Conf. Proc.* **1195**, 263–266 (2009).
- J. Zhang and T. L. Jackson, "Effect of microstructure on the detonation initiation in energetic materials," *Shock Waves* **29**, 327–338 (2017).
- T. L. Jackson, J. Zhang, and M. Short, "Multiscale approach to shock to detonation transition in energetic materials," *Propellants, Explos., Pyrotech.* **45**, 316–329 (2019).
- S. Choi, B. Kim, S. Han, and J. J. Yoh, "Multiscale modeling of transients in the shock-induced detonation of heterogeneous energetic solid fuels," *Combust. Flame* **221**, 401–415 (2020).
- R. M. Eason and T. D. Sewell, "Molecular dynamics simulations of the collapse of a cylindrical pore in the energetic material α -RDX," *J. Dyn. Behav. Mater.* **1**, 423–438 (2015).
- E. M. Escariza, J. P. Duarte, D. J. Chapman, M. E. Rutherford, L. Farbaniec, J. C. Jonsson, L. C. Smith, M. P. Olbinado, J. Skidmore, P. Foster, T. Ringrose, A. Rack, and D. E. Eakins, "Collapse dynamics of spherical cavities in a solid under shock loading," *Sci. Rep.* **10**, 8455 (2020).
- M. Ozlem, D. W. Schwendeman, A. K. Kapila, and W. D. Henshaw, "A numerical study of shock-induced cavity collapse," *Shock Waves* **22**, 89–117 (2012).
- M. S. Plesset and R. B. Chapman, "Collapse of an initially spherical vapour cavity in the neighbourhood of a solid boundary," *J. Fluid Mech.* **47**, 283–290 (2006).
- N. K. Rai, M. J. Schmidt, and H. S. Udaykumar, "Collapse of elongated voids in porous energetic materials: Effects of void orientation and aspect ratio on initiation," *Phys. Rev. Fluids* **2**, 043201 (2017).
- N. K. Bourne and J. E. Field, "Shock-induced collapse of single cavities in liquids," *J. Fluid Mech.* **244**, 225–240 (2006).
- Y. Nguyen, P. Seshadri, O. Sen, D. B. Hardin, C. D. Molek, and H. S. Udaykumar, "Multi-scale modeling of shock initiation of a pressed energetic material I: The effect of void shapes on energy localization," *J. Appl. Phys.* **131**, 055906 (2022).
- L. Michael and N. Nikiforakis, "The evolution of the temperature field during cavity collapse in liquid nitromethane. Part I: Inert case," *Shock Waves* **29**, 153–172 (2018).
- L. Michael and N. Nikiforakis, "The evolution of the temperature field during cavity collapse in liquid nitromethane. Part II: Reactive case," *Shock Waves* **29**, 173–191 (2018).
- A. B. Swantek and J. M. Austin, "Collapse of void arrays under stress wave loading," *J. Fluid Mech.* **649**, 399–427 (2010).
- E. Lauer, X. Y. Hu, S. Hickel, and N. A. Adams, "Numerical investigation of collapsing cavity arrays," *Phys. Fluids* **24**, 052104 (2012).
- N. K. Bourne and J. E. Field, "Explosive ignition by the collapse of cavities," *Proc. R. Soc. London, Ser. A* **455**, 2411–2426 (1999).
- X. C. Mi, L. Michael, E. Ioannou, N. Nikiforakis, A. J. Higgins, and H. D. Ng, "Meso-resolved simulations of shock-to-detonation transition in nitromethane with air-filled cavities," *J. Appl. Phys.* **125**, 245901 (2019).
- X. Mi, L. Michael, N. Nikiforakis, and A. J. Higgins, "Effect of spatial distribution of mesoscale heterogeneities on the shock-to-detonation transition in liquid nitromethane," *Combust. Flame* **222**, 392–410 (2020).
- N. K. Rai and H. S. Udaykumar, "Mesoscale simulation of reactive pressed energetic materials under shock loading," *J. Appl. Phys.* **118**, 245905 (2015).
- P. C. Souers, P. Lewis, M. Hoffman, and B. Cunningham, "Thermal expansion of LX-17, PBX 9502, and ultrafine TATB," *Propellants, Explos. Pyrotech.* **36**, 335–340 (2011).
- K. S. Vandersall, F. Garcia, L. E. Fried, and C. M. Tarver, "Double shock experiments and reactive flow modeling on LX-17 to understand the reacted equation of state," *J. Phys. Conf. Ser.* **500**, 052047 (2014).
- L. Michael and N. Nikiforakis, "A hybrid formulation for the numerical simulation of condensed phase explosives," *J. Comput. Phys.* **316**, 193–217 (2016).
- J. B. Bdzil, R. Menikoff, S. F. Son, A. K. Kapila, and D. S. Stewart, "Two-phase modeling of deflagration-to-detonation transition in granular materials: A critical examination of modeling issues," *Phys. Fluids* **11**, 378–402 (1999).
- C. M. Tarver, "Ignition and growth modeling of LX-17 hockey puck experiments," *Propellants, Explos. Pyrotech.* **30**, 109–117 (2005).
- C. M. Tarver and P. A. Urtiew, "Theory and modeling of liquid explosive detonation," *J. Energ. Mater.* **28**, 299–317 (2010).
- A. K. Kapila, D. W. Schwendeman, J. B. Bdzil, and W. D. Henshaw, "A study of detonation diffraction in the ignition-and-growth model," *Combust. Theory Modell.* **11**, 781–822 (2007).
- E. L. Lee and C. M. Tarver, "Phenomenological model of shock initiation in heterogeneous explosives," *Phys. Fluids* **23**, 2362 (1980).
- Z. He, Y. Ruan, Y. Yu, B. Tian, and F. Xiao, "Self-adjusting steepness-based schemes that preserve discontinuous structures in compressible flows," *J. Comput. Phys.* **463**, 111268 (2022).
- Y. Ruan, B. Tian, X. Zhang, and Z. He, "Hybrid high-order steepness-adjustable harmonic scheme based on combined discontinuity sensors," *Comput. Fluids* **241**, 105482 (2022).
- E. F. Toro, M. Spruce, and W. Speares, "Restoration of the contact surface in the HLL-Riemann solver," *Shock Waves* **4**, 25–34 (1994).